Surface & Coatings Technology 529 (2026) 133511

Contents lists available at ScienceDirect

Surface & Coatings Technology

journal homepage: www.elsevier.com/locate/surfcoat

Influence of ECO coating thickness and microstructural defects on corrosion, corrosion fatigue, and stress corrosion cracking in biomedical Mg alloys

Berzah Yavuzyegit [a,b,*], Katerina Karali [c], Sarah Davis [c], Kemal Balandiz [d], Lauren Jones [c], Nigel Smith [e], Sergey Usov [e], Pavel Shashkov [e], Roxane Bonithon [c], Gordon Blunn [a]

[a] *University of Portsmouth, School of Medicine, Pharmacy and Biomedical Sciences, Faculty of Science and Health, St Michael's Building, White Swan Road, Portsmouth, PO1 2DT, United Kingdom*
[b] *Recep Tayyip Erdogan University, Department of Mechanical Engineering, 53100, Rize, Türkiye*
[c] *University of Portsmouth, School of Mechanical & Design Engineering, Faculty of Technology, Anglesea Building, Anglesea Road, PO1 3DJ, United Kingdom*
[d] *Alten UK Innovation Laboratory, Alten Limited, 8 Pinnacle Way, Pride Park, Derby, DE24 8ZS, United Kingdom*
[e] *BioCera Medical Limited, 3b Homefield Road, Haverhill, Suffolk, CB9 8QP, United Kingdom*

ARTICLE INFO

Keywords:
Coating technology
Corrosion fatigue
Biomedical application
Corrosion mechanisms
Stress corrosion cracking

ABSTRACT

Resorbable magnesium (Mg) alloys are attractive for orthopaedic and cardiovascular implants but can degrade rapidly in physiological electrolytes, and combined corrosion–mechanical loading may trigger premature failure. Electrochemical oxidation (ECO) coatings can reduce corrosion by forming a ceramic-like surface enriched with fluoride and phosphate species, yet their brittleness raises concerns regarding integrity under concurrent corrosion and loading. Here, we investigate how ECO coating thickness influences corrosion behaviour and mechanical response under physiologically relevant conditions. AZ31 and X0 alloys were coated with 5 μm and 15 μm ECO layers and tested under static and cyclic three-point bending (3PB) in Hank's balanced salt solution (HBSS). 3PB fatigue tests revealed that cracks in the alloy initiate at the tensile surface and are associated with coating defects such as pits and cracks in the coating, or localised Ca—P deposits. Under non-corroded conditions and after 1-week of corrosion, uncoated alloy rods demonstrated slightly higher fatigue resistance and delayed crack initiation compared to coated counterparts. After 3 weeks of immersion, only the coated rods retained load-bearing capacity, with the 15 μm coating showing the longest fatigue life. Under static sustained loading, all coatings reduced crack initiation under elastic stress, whereas the 15 μm coating suppressed through-thickness crack propagation under plastic loading and thereby prevented catastrophic stress corrosion cracking (SCC)-style failure over the test duration. Overall, ECO coatings do not universally eliminate corrosion–mechanical interactions; rather, their protective efficacy is strongly condition-dependent and increases for the thicker coating under the environment–load combination examined.

1. Introduction

Magnesium alloys are increasingly considered for temporary load-sharing orthopaedic fixation devices (e.g., screws and pins), where eliminating a second operation for implant removal is a key clinical and engineering objective [1,2]. Their potential stems from the combination of biodegradability and a bone-compatible response. In particular, Mg alloys exhibit a low density (1.74–2.0 g·cm^{-3}) and an elastic modulus (41–45 GPa) that are closer to those of human bone (cortical bone: ~1.8–2.1 g·cm^{-3} and ~ 15–25 GPa) than conventional permanent implant metals [3,4] such as titanium alloys (114 GPa) and stainless steels (193 GPa) where higher stiffness promotes stress shielding due to the pronounced modulus mismatch with bone. Moreover, Mg-based devices are intended to interact with physiological fluids and

---

* Corresponding author at: University of Portsmouth, School of Medicine, Pharmacy and Biomedical Sciences, Faculty of Science and Health, St Michael's Building, White Swan Road, Portsmouth, PO1 2DT, United Kingdom.

E-mail addresses: berzah.yavuzyegit@port.ac.uk, berzah.yavuzyegit@erdogan.edu.tr (B. Yavuzyegit), katerina.karali@port.ac.uk (K. Karali), sarah.davis@port.ac.uk (S. Davis), kemal.balandiz@alten.co.uk (K. Balandiz), lauren.jones2002@live.co.uk (L. Jones), nigel.smith@biocera-med.com (N. Smith), sergey.usov@biocera-med.com (S. Usov), pavel.shashkov@biocera-med.com (P. Shashkov), roxane.bonithon@port.ac.uk (R. Bonithon), gordon.blunn@port.ac.uk (G. Blunn).

https://doi.org/10.1016/j.surfcoat.2026.133511
Received 29 January 2026; Received in revised form 16 April 2026; Accepted 18 April 2026

gradually convert to ionic species through corrosion, enabling temporary mechanical support followed by resorption rather than long-term retention [5].

Despite these advantages, Mg can degrade too rapidly in vivo, with corrosion accompanied by hydrogen gas evolution [6]. This can trigger premature loss of mechanical integrity and may lead to gas pockets and local tissue irritation, potentially impairing peri-implant bone quality and reducing fixation strength [2,7]. This limitation is particularly critical for load-sharing fixation, where implants are continuously exposed to physiological electrolytes and must sustain substantial mechanical demands [8–10]. In chloride-containing physiological media, Mg alloys are also susceptible to localised corrosion, particularly pitting. Once pits grow beyond a critical size, they act as dominant stress concentrators that can promote stress corrosion cracking (SCC) under sustained tensile stress and cyclic loading [11,12]. These coupled mechanical–electrochemical damage modes can shorten the effective service life of an implant more severely than corrosion-driven section loss alone, thereby increasing the risk of failure during function [13,14]. This is clinically relevant because bone healing progresses through inflammatory, reparative, and remodelling phases, and during the reparative stage, the newly formed callus has limited load-bearing capacity [15,16]. Therefore, temporary fixation devices must retain sufficient mechanical integrity in the physiological environment until stable healing is achieved [17]. Moreover, SCC of Mg alloys has been associated with transgranular cracking driven by hydrogen-assisted embrittlement alongside anodic dissolution, indicating that corrosion-generated hydrogen can accelerate crack initiation and growth [18,19]. Collectively, these processes make it challenging to maintain adequate implant stability throughout the healing period and therefore evaluation of Mg alloys under combined loading and physiologically relevant environments is important.

To mitigate the rapid degradation and environmentally assisted cracking susceptibility of Mg alloys, surface modification has emerged as a practical and widely investigated strategy [20–22]. Among these approaches, plasma electrolytic oxidation (PEO), also referred to as micro-arc oxidation (MAO), has been widely adopted because it can generate hard, ceramic-like oxide layers that initially slow electrolyte ingress and improve corrosion resistance in chloride-containing media [23,24]. However, the protective performance of PEO/MAO coatings is intrinsically constrained by their characteristic microporous and microcracked morphology predominantly caused by uncontrolled micro-arching [25]. These inherent defects act as preferential pathways for electrolyte penetration and, critically, may widen and interconnect under mechanical loading [26]. Under sustained or cyclic stresses, stress concentration at pore edges and crack tips can promote further cracking and local debonding, such that the brittle PEO/MAO coating may fail prematurely during environmentally assisted cracking (e.g., SCC), thereby limiting its long-term ability to protect the underlying Mg substrate [26–28]. Consequently, there is increasing interest in coatings that retain the corrosion-mitigation benefits of anodic oxide layers while improving their tolerance to crack propagation under load, motivating the exploration of alternative electrochemical oxide approaches such as electrochemical oxidation (ECO) coatings.

ECO represents a modified high-energy anodic oxidation route developed to address key limitations of conventional PEO/MAO coatings [29]. In ECO, the electrical input is tailored to minimize micro-arcing while maintaining the energy required for ceramic layer formation, achieved through bipolar voltage pulsing, trapezoidal pulse shapes, and programmed control of process parameters such as pulse repetition frequency, duty cycle, and ramping modes. In our previous work, ECO coatings with controlled thickness were shown to markedly improve corrosion resistance in aggressive chloride media (5 M NaCl), with the 15 μm coating yielding substantial reductions in corrosion indicators compared with thinner coatings and uncoated AZ31, as evidenced by both time-dependent mass-loss measurements (up to ~35-fold reduction after 2 weeks in NaCl) and electrochemical assessments (up to ~80-fold reduction inferred from Tafel-based metrics) [29,30]. Nevertheless, for load-sharing applications, corrosion resistance must be considered alongside coating integrity under mechanical loading. Using high-resolution digital image correlation (HR-DIC) combined with SEM, we recently quantified crack initiation and evolution in phosphate- and fluorine-rich ECO coatings on AZ31 during three-point bending in both non-corrosive and physiological environments [31]. That study revealed a thickness-dependent cracking response and demonstrated that, under sufficiently high loading, cracks can propagate through the full coating thickness. In addition the ECO process produces a non-smooth coating–substrate interface and these local coating discontinuities can act as micro-notches at the tensile surface, elevating local stresses and facilitating early crack nucleation. These observations underscore a key mechanistic tension: although anodic-oxide coatings can reduce general corrosion, defect evolution and stress concentration within the coating and at the interface can govern fatigue and SCC performance under coupled mechanical–electrochemical conditions.

Despite growing interest in anodic-oxide coatings for Mg alloys, a key unresolved issue is how improvements in corrosion resistance translate into performance under service-relevant mechanical loading in physiological environments [31]. In particular, the coupled influence of coating thickness (e.g., 5 vs 15 μm), corrosion history (conditioning time), and coating defects (pores, microcracks, scratches, and through-thickness cracking) on crack initiation and propagation under bending-dominated loading in physiological environments remains underexplored. Moreover, many studies emphasise corrosion-only immersion metrics and often rely on gravimetric measurements, which can be confounded by adherent corrosion products, whereas assessments that integrate coatings with SCC-relevant loading are limited. Addressing these gaps is essential to identify coatings that preserve mechanical integrity throughout the bone-healing period under coupled mechanical–electrochemical conditions.

Accordingly, this study aims to quantify the influence of ECO coating thickness on the corrosion and mechanically assisted degradation of Mg alloys considered for biomedical use. Two Mg alloys (AZ31 and X0) were investigated in uncoated and ECO-coated conditions, using two controlled coating thicknesses (5 μm and 15 μm). Corrosion severity was quantified by paired X-ray computed tomography (XCT) scans acquired before and after immersion in Hank's Balanced Salt Solution (HBSS), enabling volumetric loss measurements that are not biased by retained corrosion products. Mechanical integrity under physiological exposure was evaluated using cyclic three-point bending (3 PB) in HBSS to assess fatigue and susceptibility to stress corrosion cracking (SCC) under sustained tensile stress, supported by post-fracture examination to identify crack initiation features and coating/substrate failure modes. We hypothesise that while thicker ECO coatings can reduce electrolyte access and lower corrosion damage, fatigue and SCC performance will depend strongly on defect evolution and crack connectivity within the coating; consequently, corrosion reduction and improved mechanical lifetime under coupled mechanical–electrochemical conditions will be idiosyncratic and can only be predicted by testing under realistic conditions.

2. Materials and methods

2.1. Materials and sample preparation

Two types of magnesium alloys were used in this study: AZ31 (nominal composition: 3 wt% Al, 1 wt% Zn, balance Mg) and X0 (0.45 wt% Ca, balance Mg). AZ31 alloy was supplied in the form of extruded bars and machined into cylindrical rods with a diameter of 3 mm and a length of 115 mm, incorporating a 5 mm threaded section at one end to facilitate immersion during the coating process. X0 alloy specimens were supplied by Kairos Medical AG (Bettlach, Switzerland), and machined from extruded barstock to a diameter of 3 mm and a length of 35 mm. Table 1 presents the measured concentrations of trace elements

Table 1
Concentration of trace elements in the X0 alloy determined by Glow Discharge Mass Spectrometry. Only elements with concentrations greater than 1 ppm are included. All values are reported in ppm.

Si	P	Mn	Fe	Zn	Pb
1.3	4.9	1.2	1.3	15	1.1

in the X0 alloy.

Both AZ31 and X0 alloy rods were coated by BioCera Medical Ltd. (Haverhill, UK) using a proprietary Electrochemical Oxidation (ECO) technique derived from a soft-sparking Plasma Electrolytic Oxidation (PEO) process, patented by the company (PCT publication WO 2020049299). This advanced method minimizes the intensity of discharge events by alternating between potentiostatic and galvanostatic control modes, thereby limiting breakdown sparking and promoting the formation of a denser, more uniform ceramic-like surface layer. Coatings were applied using a phosphate–fluoride (PF) electrolyte system, formulated with low concentrations of phosphates (typically <5 g/L) and alkali metals. The electrolyte conductivity was maintained at 25 $mS \cdot m^{-1}$, regulated by the addition of potassium hydroxide (KOH). The inclusion of phosphate supports biocompatibility and mechanical integrity, while fluoride contributes to layer compaction and may offer antibacterial effects.

Two coating thicknesses, 5 μm and 15 μm, were prepared and applied to AZ31 and X0 alloys. Details regarding the preparation of specimens for microstructural characterisation, including SEM and EDX analysis, are provided in Section 2.5. After coating, AZ31 rods were sectioned into 35 mm-long specimens using a fine-toothed hacksaw to minimize surface damage, whereas X0 alloy specimens were coated directly in 35 mm lengths. To prevent localised corrosion and eliminate galvanic effects during immersion testing, both ends of each specimen were sealed with epoxy resin.

2.2. Corrosion conditioning protocols

Rods were immersed in HBSS (Gibco, Thermo Fisher, USA) to simulate physiological fluid. HBSS is a commonly used solution that mimics the ionic composition of human extracellular fluid. The purpose of this procedure was to induce condition the test articles prior to fatigue testing and to quantify corrosion rates in specimens subjected to 3-week immersion. Our previous findings have demonstrated that the corrosion rate of ECO-coated samples in HBSS is negligible [31].

Prior to immersion, all samples were ultrasonically cleaned in 99% ethanol using a digital ultrasonic bath (XUBA3, Grant Instruments, Cambridgeshire, UK) for 15 min, followed by air drying at room temperature for 30 min to ensure removal of surface contaminants. Each rod was then fully submerged in 100 mL of HBSS, maintained at ambient laboratory temperature (~22 °C), and placed on an orbital shaker (Orbi-Shaker, Benchmark Scientific, USA) operating at 30 rpm to ensure gentle fluid circulation and uniform exposure. The immersion time in HBSS was applied depending on the experimental group: 1 week and 3 weeks. Following immersion, specimens were again ultrasonically cleaned in ethanol and air dried to remove corrosion products prior to subsequent testing or analysis.

2.3. X-ray computed tomography imaging

X-ray computed tomography (XCT) imaging was conducted to quantify corrosion-induced material loss in AZ31 specimens (uncoated, 5 μm and 15 μm coated) immersed in HBSS for 3 weeks ($n = 3$). Imaging was conducted using a high-resolution XCT system (Xradia 520 Versa, Zeiss, USA), operating at an acceleration voltage of 40 kV, with a power setting of 3 W. A LE1 filter was applied, and scans were acquired with 1.25 s exposure, over 2401 projections, at a voxel resolution of 35 μm. These parameters were kept constant for both pre- and post-immersion scans to ensure consistency in volumetric analysis.

To avoid interference from surface sealing materials, a central region of the rod (sufficiently distant from the epoxy-sealed ends) was selected for scanning. This ensured that the analysis focused solely on the corrosion-affected metal without artefacts caused by boundary conditions or edge effects.

Pre and post-immersion scans were aligned using image registration in Avizo software (Thermo Fisher Scientific). A standardised image processing workflow was applied, including subvolume extraction and interactive thresholding, followed by segmentation. Identical parameters were used for both scan sets to maintain analytical consistency. The corrosion rate C was calculated using the following formula:

$$C = \frac{\Delta V}{AT} \tag{1}$$

where ΔV is the change in volume (mm^3), T is the immersion time (in years), and A is the initial surface area of the specimen (mm^2). The final corrosion rate is reported in mm/year.

2.4. Mechanical testing

2.4.1. Force-controlled (monotonic) 3 PB testing

Three-point bending (3 PB) tests were performed using a Bose ElectroForce 3200 with an in-house acetal (polyoxymethylene, POM) fixture designed for both quasi-static and fatigue loading (Fig. 1a). The same fixture and pin geometry were used throughout to ensure identical support conditions and boundary constraints. All specimen-contact components were manufactured from acetal to avoid galvanic coupling with magnesium during immersed testing.

The fixture incorporated two parallel acetal guide rods to maintain coaxial alignment between the central loading jig and the supports during actuation. Load from the Bose actuator was transmitted directly to the central loading pin through a rigid vertical rod, without a load-spreading adapter. Specimens (AZ31 and X0) were supported on two cylindrical acetal pins (Ø3 mm) at a 30 mm span, with loading applied at mid-span. Specimen length was 35 mm, providing minimal overhang.

To minimize micro-slippage during long runs, a thin strip of double-sided adhesive film was applied to the support pins immediately before mounting each specimen. Unless stated otherwise, immersed quasi-static tests were conducted at ambient laboratory temperature with the specimen fully submerged in HBSS (100 mL per specimen); this solution was not renewed during testing. A 10 mm-thick, custom-machined acetal base disk, contoured to the container footprint, was installed beneath the fixture to distribute loads and preserve alignment; the disk incorporated guide-rod holes and drainage perforations. For immersed tests, specimen ends were epoxy-masked to minimize crevice/galvanic effects.

Monotonic tests were run in force control at a loading rate of 1 $N \cdot s^{-1}$ up to 150 N. For each alloy, $n = 3$ specimens were tested. The nominal bending stress on the surface of the rods was calculated using the equation for a cylindrical section and was estimated as:

$$\sigma_{max} = \frac{8FL}{\pi d^3} \tag{2}$$

which for L = 30 mm and d = 3 mm corresponds to ≈141 MPa at 50 N and ≈424 MPa at 150 N. These results informed the fatigue peak-load selection.

2.4.2. 3 PB fatigue testing

Fatigue tests used the same fixture and geometry (Ø3 mm acetal pins, 30 mm span; acetal loading pin). Tests were conducted in load control with a sinusoidal waveform between 5 N and 50 N at 1 Hz ($R = F_{min}/F_{max} = 0.10$; mean load 22.5 N; amplitude 27.5 N). The 50 N peak was chosen to remain in the elastic regime for the tested geometry/material (Section 2.4.1). Tests were either in air or fully immersed in HBSS at ambient

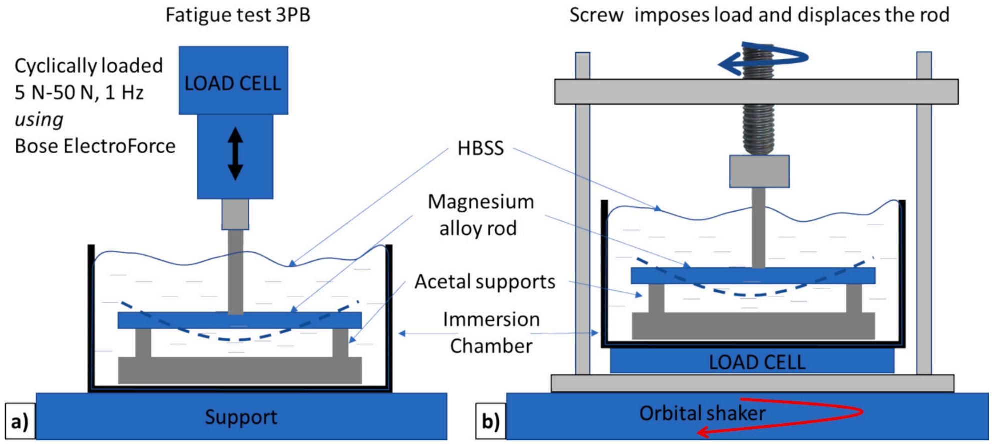

Fig. 1. Three-point bending fixtures and test configurations. (a) Quasi-static and fatigue three-point bending setup mounted on a Bose ElectroForce 3200 system. (b) Static sustained-load (constant-displacement) three-point bending rig.

laboratory temperature. All contact elements were acetal, and ends of immersed specimens were sealed using an epoxy-mask.

Tests were terminated upon fracture or by run-out, defined a priori as no change in actuator (loading-rod) displacement at the prescribed load after 150,000 cycles. In a subset of specimens, loading was intentionally extended beyond 150,000 cycles to assess the effect of an increased number of cycles; these runs were stopped either at fracture or at a predefined time. Runs that ended without fracture were recorded as run-outs in the dataset.

In selected specimens, testing was paused at intermediate cycle counts (e.g., 25,000 cycles) to enable early-stage damage assessment before resuming or terminating the test. Three conditions were investigated: non-corroded, pre-corroded samples incubated in HBSS for 1 week (1 W) and for 3 weeks (3 W) before testing. Unless otherwise stated, $n = 4$ specimens were tested for each alloy and for each condition. The testing scheme is summarised in Table 2.

2.4.3. *Displacement-controlled (quasi-static) 3 PB test*

Cylindrical rods (d =3 mm) were prepared as reported in Section 2.1, and the ends of the rods were epoxy-masked. Each test was performed in 100 mL HBSS per specimen, in an open-top container on an orbital shaker (30 rpm) at ambient laboratory temperature; the solution was not renewed over 14 days. A custom static 3 PB rig was constructed to apply sustained bending under immersion using the same geometry as used in the fatigue tests (two acetal supports, Ø3 mm; 30 mm span; central acetal loading pin) (Fig. 1b). Loading was applied using a fine-pitch mechanical screw (M14, pitch 1 mm), establishing constant-displacement. The applied force was transmitted through a thrust bearing mounted between the screw and the rig. Before each test, the load cell was calibrated at 100 g. The system response was tested to confirm stable and accurate, monotonic readings within the 1–5 kg range. The force was monitored via an inline load cell connected to an Arduino-based display. All contact components were acetal.

Table 2
Number of AZ31 and X0 Mg alloy rods used for the fatigue testing both as received and following short duration conditioning to corrode articles. Asterisks (*) indicate the subset of specimens used for corrosion rate quantification via XCT.

	Non-Corroded		1 W pre-corroded in HBSS		3 W pre-corroded in HBSS	
	AZ31	X0	AZ31	X0	AZ31	X0
Uncoated	4	2	4	4	3*	N/A
5 μm coated	4	N/A	4	4	3*	N/A
15 μm coated	4	N/A	4	4	3*	N/A

Forces of 50 N (elastic regime) and 150 N (plastic onset and beyond) were selected based on the force displacement data. Using the nominal stress calculation in Eq. (2) above these correspond to ≈141 MPa and ≈424 MPa, respectively, for $L = 30$ mm and $d = 3$ mm. The screw position was adjusted to reach the desired force (verified on the Arduino display). Load was checked at 30 and 60 min and subsequently twice daily, and minor manual adjustments were made if drift was observed.

2.5. *Characterisation of surface and cross-sectional morphologies*

Following ECO coating and mechanical testing, surface and cross-sectional characterisation of both AZ31 and X0 alloy rods was conducted to evaluate coating morphology, structural integrity, corrosion-related degradation, and fracture behaviour. Analyses were performed on uncorroded coated samples as well as specimens that had undergone fatigue testing and/or corrosion exposure.

Fractured specimens were divided into two parts: one part of the fractured rod was used to examine the fracture surface, while the other part was embedded in cold-curing epoxy resin for cross-sectional analysis. Mounted samples were sequentially ground with silicon carbide abrasive papers (grit sizes 800, 1200, and 2500) and polished using a 1 μm and 0.25 μm diamond suspension. Between each step, samples were ultrasonically cleaned in 99% ethanol for 5 min and air dried to ensure a clean, debris-free surface.

Prior to SEM imaging, all specimens were sputter-coated with a ~ 10 nm carbon layer to improve surface conductivity and reduce charging under vacuum. Imaging was performed using a ZEISS Sigma 300VP field-emission SEM under high-vacuum conditions. A working distance of 12 mm was used for SE and BSE imaging, and 15 mm for EDX analysis. Images were acquired using both secondary electron (SE) and back-scattered electron (BSE) detectors at accelerating voltages of 5–10 kV, depending on resolution and contrast requirements.

Elemental characterisation was carried out using Energy-Dispersive X-ray Spectroscopy (EDX) with an Oxford Instruments detector. EDX analyses were conducted in both point and mapping modes at an accelerating voltage of 15 kV and a working distance of 15 mm. The distribution of Mg, Al, Zn, P, F, and Ca was evaluated to determine coating homogeneity, elemental penetration, and signs of corrosion-induced changes at the coating–substrate interface.

In addition to fully fractured specimens, several samples were intentionally removed from fatigue testing (e.g., at 25,000 cycles) to investigate early-stage damage. These were cross-sectioned and analyzed for subsurface cracking, coating delamination, and corrosion-assisted crack initiation, with specific attention paid to the tensile surface of the bending region, where crack formation was expected.

2.6. Statistical analysis

All quantitative data obtained from fatigue and corrosion testing were subjected to statistical analysis to assess the significance of observed differences between groups. Due to the limited number of samples and non-normal distribution of the datasets, nonparametric tests were employed.

The Kruskal–Wallis H test was used to evaluate differences among multiple independent groups, including different coating thicknesses and corrosion conditions. Where significant differences were detected, post-hoc pairwise comparisons were conducted using the Mann-Whitney *U* test with Bonferroni correction to control for multiple comparisons.

Repeated measures two-way ANOVAs with Bonferroni multiple comparisons tests were used, where sphericity was not assumed, for testing differences in load reduction between coated and non-coated groups from the static loading tests.

Statistical significance was defined as $p < 0.05$. Descriptive statistics, including mean, standard deviation, and range, were calculated for each group and presented alongside the graphical data. All analyses were performed using IBM SPSS Statistics software (IBM Corp., Armonk, NY, USA) or GraphPad Prism (Version 8.02, GraphPad, San Diego, California, USA).

3. Results

3.1. As-coated microstructure and composition

Surface and cross-sectional SEM images of ECO-coated AZ31 and X0 specimens with nominal thicknesses of 5 μm and 15 μm are shown in Fig. 2. The 5 μm coatings exhibited a comparatively smoother and more uniform surface, whereas the 15 μm coatings displayed a rougher and uneven morphology, and this is in agreement with our previous work [29]. The pores in the 15 μm coatings appeared larger than those in the 5 μm coatings [30]. Surface images highlighted open pores, each surrounded by a rim of coating material. Cross-sectional views confirmed that surface pores and cracks extended through the porous outer region of the coating down to a thin dense interfacial layer of approximately 1 μm (Fluoride-rich) adjacent to the substrate. The ECO process eroded the alloys, but this dense coating layer was continuous across the undulating alloy surface, and no evidence of delamination or loss of adhesion was observed.

In contrast, additional localised features were identified on the ECO-coated X0 specimens. As shown in Fig. S 1, the X0 coating surfaces exhibited localised nodular surface irregularities superimposed on the porous oxide matrix for both the 5 μm and 15 μm coatings. SE and BSE imaging suggested that these regions correspond to locally reduced coating thickness; however, they were distributed over the surface and observed in both coating conditions. Moreover, cross-sectional imaging of X0 revealed interfacial separation/delamination together with a transverse coating crack (Fig. S 1b). Notably, no comparable surface irregularities or delamination were observed on the ECO-coated AZ31 specimens under the examined conditions.

3.2. Loading morphology after 3 weeks corrosion via XCT

Corrosion rate was quantified by paired XCT scans acquired before and after a 3-week immersion in HBSS (Fig. 3). The key advantage of XCT is that it enables direct quantification of volumetric material loss without bias from corrosion products retained on the surface, which can mask mass loss and reduce the accuracy of gravimetric measurements. In our previous study [31], gravimetric weight-loss measurements showed no measurable mass loss up to 2 weeks for both non-coated and ECO-coated AZ31; therefore a 3-week interval was selected here to obtain direct corrosion rate measurements using volumetric change obtained using XCT rather than gravimetric measurements (Fig. 3).

It was observed that most of the coated specimens exhibited pronounced corrosion at both ends, particularly at the epoxy-sealed regions. The ECO coating reduced the mean corrosion rate substantially, decreasing from 5.27 mm/year in the uncoated condition to 0.19 mm/year and 0.11 mm/year for the coated conditions (5 μm and 15 μm, respectively). However, due to the large scatter in the uncoated group and the limited number of valid specimens (one uncoated rod fully degraded before the post-immersion scan), the overall differences were not statistically significant (Kruskal–Wallis, $p = 0.119$). Excluding the near-completely corroded uncoated specimen (uncoated-2) did not change this conclusion, as the uncoated group then comprised only two data points, limiting statistical power.

Within the coated sets, one specimen (5 μm-coated specimen 3) exhibited a higher corrosion rate than the other coated rods, which was traced to a pre-existing scratch/defect in the coating, consistent with locally accelerated attack through a compromised barrier. Overall, these results indicate that ECO coating is effective in reducing the severity of corrosion, while local coating damage can dominate the response in individual specimens. The morphology of the uncoated specimens was consistent with corrosion showing rods of reduced diameter with an undulating and pitted surface whereas the coated rods remained smooth and had an even diameter.

3.3. Quasi-static 3 PB response

Representative force–displacement and flexural stress–strain curves are shown in Fig. 4a–b. Both alloys exhibit similar elastic slopes, giving an apparent flexural modulus of ≈25 GPa. Consistent with our previous work coating does not seem to affect the stiffness of the rods, where coated and uncoated AZ31 showed a similar deformation in the linear elastic region. In Fig. 4, only the AZ31 (15 μm) condition is plotted for clarity. Because of the instrument limit (150 N), the X0 alloy (uncoated, 5 μm, 15 μm) was loaded in the elastic limit and did not show a yield

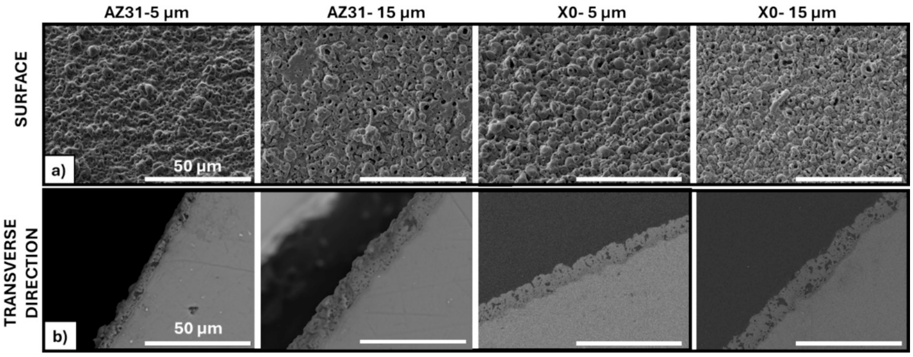

Fig. 2. Surface and cross-sectional SEM images of ECO-coated AZ31 and X0 specimens with nominal coating thicknesses of 5 μm and 15 μm. (a) SE surface images. (b) Cross-sectional BSE-SEM images. Scale bars are 50 μm in all panels.

	Corrosion Rate (CR)	MicroCT image
AZ31-uncoated	5.27 ± 5.19 mm/year	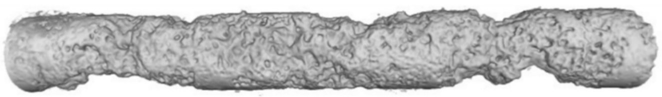
AZ31-5 μm	0.19 ± 0.24 mm/year	
AZ31-15 μm	0.11 ± 0.07 mm/year	

2 mm

Fig. 3. Mean ± standard deviation corrosion rate of AZ31-uncoated, −5 μm, and − 15 μm after 3-week immersion in HBSS and their corresponding XCT images. The units are mm/year.

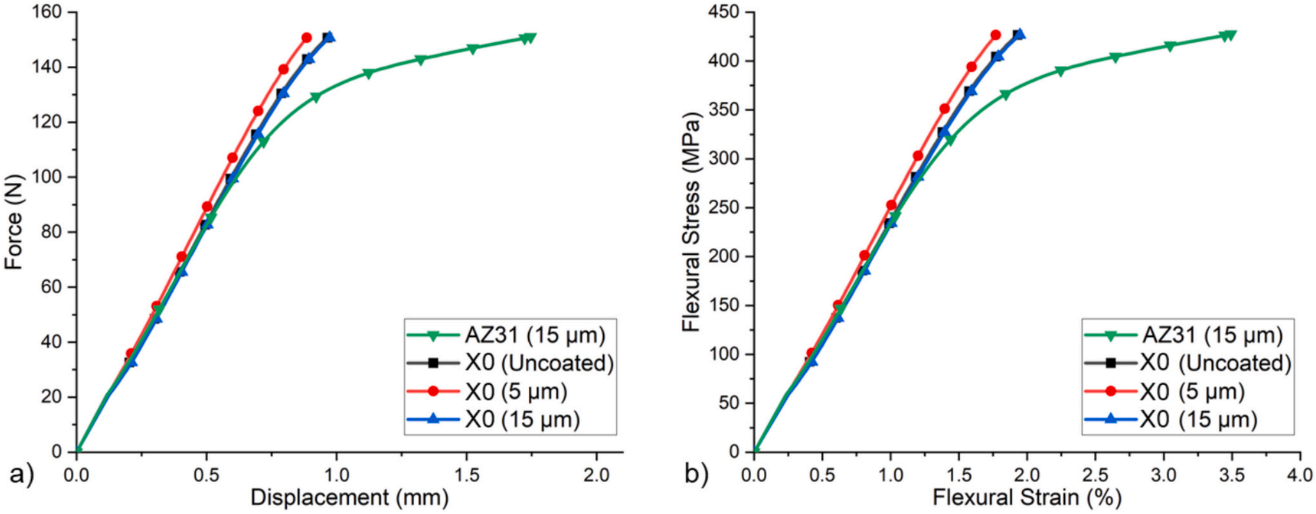

Fig. 4. (a) Force–displacement and (b) flexural stress–strain curves for AZ31 (15 μm ECO) and X0 (uncoated, 5 μm, 15 μm) tested in 3 PB.

point ($\sigma > 424$ MPa), whereas AZ31 showed clear plasticity above ~125 N ($\sigma \sim 350$ MPa). Coating thickness on X0 (5 vs 15 μm) produced no measurable change in elastic slope. As indicated in the Methods, 50 N lies well within the linear regime for both alloys (≈141 MPa equivalent stress), supporting its use as the peak load in the fatigue protocol.

3.4. 3 PB fatigue life at constant amplitude

The fatigue life of AZ31 and X0 Mg alloy rods after different immersion times in HBSS is presented in Fig. 5. Tests of rods that were not immersed in HBSS (dry environment) at the same loading (peak 50 N, $R = 0.10$, 1 Hz) produced run-out at 2×10^5 cycles for both AZ31 and X0; fatigue testing in air was therefore not pursued further. All results refer to immersed conditions.

For AZ31 (non-corroded controls), the mean number of cycles at fatigue failure (N_f ± SD) were 50,000 ± 9000 (uncoated), 39,000 ± 8000 (5 μm coated), and 52,000 ± 12,000 cycles (15 μm coated). After 1-week immersion in HBSS, the uncoated and 5 μm-coated AZ31 specimens exhibited fatigue lives comparable to or marginally higher than their non-corroded controls, whereas the 15 μm coating did not provide an improvement, showing a slight reduction relative to the control. After 3 weeks of immersion, behaviour diverged: uncoated specimens had fully degraded prior to fatigue loading (no meaningful N_f), while 15 μm coated specimens achieved the highest AZ31 life within that duration. Overall, AZ31 did not show a dependence on coating thickness across both immersion times and nonparametric tests did not detect significant differences within AZ31 pre-corroded thickness groups ($p > 0.05$).

By contrast, X0 exhibited substantially longer fatigue lives at the same load. In the non-corroded, uncoated X0 samples (two tests), both specimens were stopped without failure at 127,000 and 316,000 cycles (right-censored run-outs). After 1-week in HBSS, uncoated X0 failed within 66,000–203,000 cycles; for 5 μm coated X0, one specimen failed at 233,000 cycles, while the remaining coated samples were run-outs at 165,000–193,000 cycles; 15 μm coated X0 showed no failures within 239,000–281,000 cycles (all run-outs). A Kruskal–Wallis comparison across the pre-corroded X0 thickness groups was significant ($p = 0.021$), with a significant uncoated vs 15 μm coated contrast ($p = 0.024$).

3.5. The effect of static load

Static constant-displacement 3 PB tests were performed on uncoated and 15 μm coated AZ31 samples in HBSS at target loads of 50 N (elastic loading) and 150 N (plastic loading) (Fig. 6). At 50 N, non-coated and 15 μm coated samples showed a steep decline in load between days 1 and 2, followed by a gradual decline thereafter (Fig. 6a). By day 14, the load had fallen from ~5.1 kg (≈ 50 N) to ~3.3–3.7 kg (≈ 33–36 N), i.e., a ~ 30–35% reduction, with overlapping variability and no significant differences between uncoated and 15 μm coated specimens. No specimen failure was observed at this load. Gas evolution (bubbling) was frequently visible around uncoated specimens during immersion.

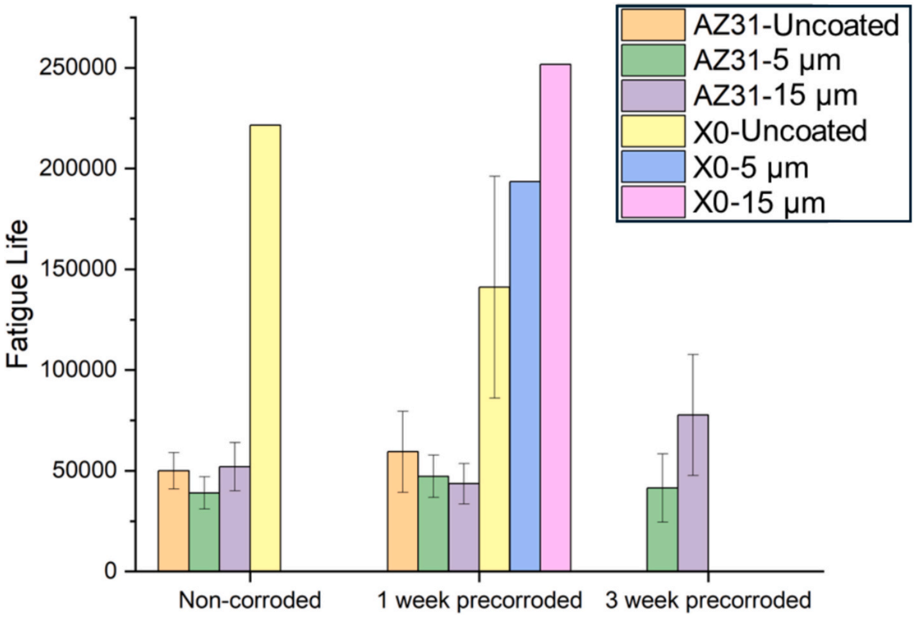

Fig. 5. Fatigue life (cycles to failure, *N f*) under constant-amplitude three-point bending for AZ31 and X0. Bars show group means ± SD for non-corroded, 1 week of pre-corroded, and 3 weeks of pre-corroded specimens in the uncoated, 5 μm coated, and 15 μm coated conditions. Uncoated AZ31 (3 weeks) fully degraded before fatigue testing. Due to a limited number of specimens, standard errors for coated X0 alloys corroded for 1 and 3 weeks before testing could not be calculated.

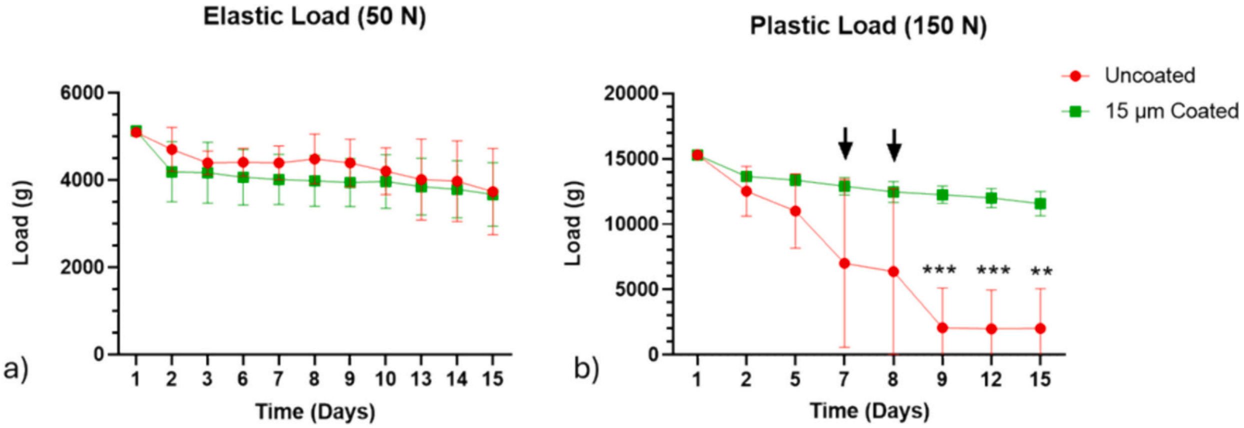

Fig. 6. Static sustained-load response of AZ31 during immersion in HBSS. (a) Load response after an initial load of 50 N for uncoated and 15 μm coated specimens. (b) Load response after an initial load of 150 N for uncoated and 15 μm coated specimens; black arrows indicate fracture events. Data are presented as mean ± SD, with ** $p = 0.0016$ and *** $p < 0.001$.

With a plastic load of 150 N, the two conditions diverged markedly (Fig. 6b). 15 μm thick coated samples retained most of the applied load, decreasing from ~15.3 kgf (≈ 150 N) to ~11.5–12.0 kgf (≈ 115–120 N) over 14 days (~25% reduction) without fracture. In contrast, non-coated samples exhibited stepwise load loss with abrupt drops between day 5 to 9, stabilising at ~2.0–2.5 kgf (≈ 20–25 N) and with sample failure occurring at days 7 and 9.

3.6. Fractography and damage mechanisms

3.6.1. Fatigue tests (AZ31)

Fracture surfaces from all AZ31 conditions showed initiation of cracks on the tensile surface and crack growth from the tensile side toward the compressive (loading-pin) side (Fig. 7a1–c1). In each case, a small, comparatively smooth initiation zone was observed at the tensile edge, followed by a rapid transition to a dimpled morphology associated with final overload. In all the specimens, the origin surface at the tensile edge was smooth; whereas in fracture specimen, shallow surface imperfections/pits coincided with the initiation site. In the 15 μm coated specimens, no interfacial delamination was evident at the origin. The 15 μm coated AZ31 samples that were pre-corroded in HBSS for 1 week (Fig. 7c1–c2) displayed abundant microvoids. No evidence of classical concentric fatigue striations was observed on any fracture surface.

Higher-magnification images of the microstructure shown in Fig. 7a1 are provided in Supplementary Fig. S 2: (a) a mid-thickness transition area showing mixed fatigue-growth features with emerging dimples, (b) the neutral-axis region with comparatively smooth fatigue morphology, and (c) the final-overload core just beyond the neutral axis on the compression side, characterized by equiaxed dimples from microvoid coalescence. These views illustrate the progression from smooth early fatigue growth at the tensile edge to a dimpled overload area as the crack traverses the section.

BSE/EDS analysis of an AZ31 cross-section taken at the tensile side after 3 PB fatigue in HBSS shows local by Ca—P deposits over the surface (Fig. 8). The crack-origin lies at the tensile edge adjacent to these deposits and there is no evidence of a continuous Mg-oxide/hydroxide

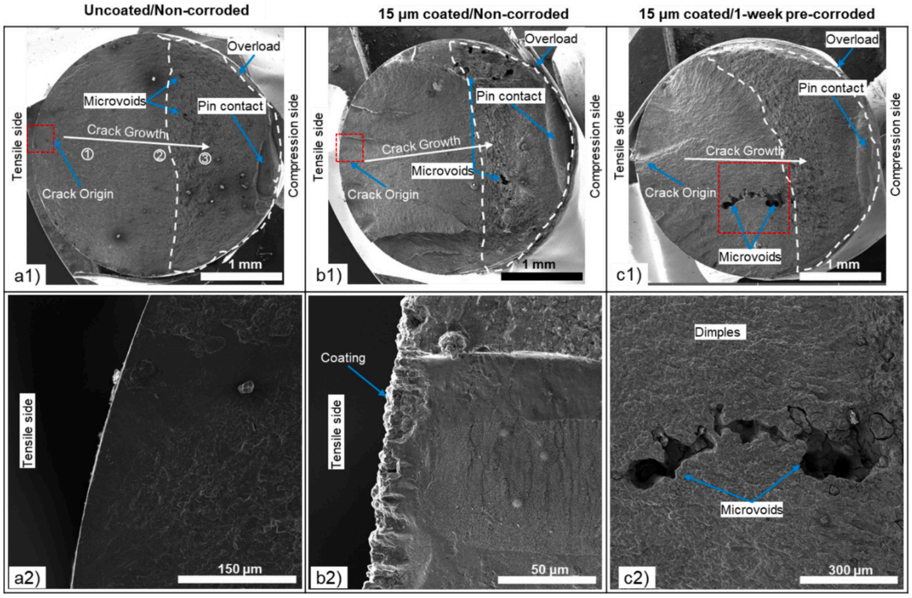

Fig. 7. Fatigue fracture surfaces and initiation morphologies of AZ31 rods tested 3 PB. Top row (a1–c1): whole-section views with the tensile side on the left and the loading-pin (compressive) side on the right; the neutral axis is indicated by a dashed line and the peripheral final overload (shear-lip) rim is outlined. (a1) Uncoated, non-corroded, (b1) 15 μm ECO, non-corroded, and (c1) 15 μm ECO, 1-week pre-corroded in HBSS. Bottom row (a2–c2): corresponding high-magnification details (a2) tensile-edge origin area in uncoated non-corroded, (b2) crack initiation of 15 μm coating and non-corroded, and (c2) microvoid coalescence representative of the final-overload region. 1–2-3 in a1 refer to the regions investigated at high resolution in Fig. S 2.

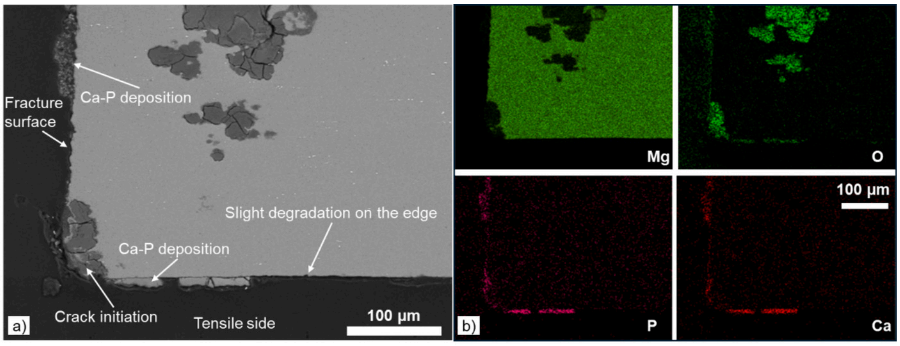

Fig. 8. BSE cross-section and EDS elemental maps in the tensile region of AZ31 specimen after 3 PB fatigue in HBSS. (a) BSE image of the tensile-edge region. (b) EDS maps of the same field of view for Mg, O, P, and Ca.

scale; instead, the chemistry is dominated by apatite-like Ca—P precipitation. In the BSE image (Fig. 8a) bright plate-like islands are on the surface and correspond to regions where Ca and P are co-localised as shown in EDS maps, while the Mg is absent in these regions (Fig. 8b). Also, the dark peripheral band is oxygen rich and is consistent with embedding resin that has infiltrated the edge rather than with $Mg(OH)_2$/MgO. The metallic matrix exhibits a uniform Mg map, indicating no pervasive subsurface degradation.

Surface and cross-sectional analyses reveal the local damage that precedes fatigue failure (Fig. 9). A 5 μm ECO-coated, non-corroded intact AZ31 rod was taken off test at 25,000 cycles prior to final fracture, mounted, sectioned, and polished. SEM of the tensile-side region close to the loading pin revealed regular, needle-like crack precursors located within the coating and immediately beneath it in the substrate (Fig. 9a). EDS maps showed these features to be oxygen-enriched with trace Ca (≈ 1 wt%) (Fig. 9b1–b2). Along the coating–substrate interface, a corrosion-affected interfacial region was evident (Fig. 9a), where the Mg signal was reduced relative to the adjacent matrix; notably, no continuous interfacial delamination was observed.

In a separate specimen with a 15 μm coating, fracture occurred after 59,000 cycles, and the tensile surface showed similar needle-like crack precursors (Fig. 9c).

3.6.2. *Fatigue tests (X0)*

Fig. 10 shows the fracture surface and chemistry of a X0 Mg alloy immersed in HBSS for 1 week before the test. After failure in 3 PB, the whole-section view shows a tensile-side crack origin with growth toward the compression side, bounded peripherally by a shear-lip (overload) rim; the pin-contact imprint is evident (Fig. 10a). In Area 1 near the tensile edge, the fracture surface is covered by speckled deposits; EDS maps reveal O–P–Ca enrichment with local Mg depletion, consistent with Ca—P deposition on the surface (Fig. 10b1–b2). In Area 2, located close to the neutral axis, the fracture surface contains microcrack arrays that run across the field and locally intersect the main crack (Fig. 10c). Area 3, taken at the edge near the neutral axis, exhibits a composition gradient: the interior appears Mg-rich, while the outer rim shows Ca—P enrichment on the fracture surface (Fig. 10d).

X0 alloy specimens without coating and without immersion in HBSS did not fracture within the prescribed life. A cross-section prepared from a specimen interrupted at 127,000 cycles revealed a dominant crack initiation at the tensile edge advancing toward the compression side with branching at the tip (Fig. 11a). In the tensile region just below the

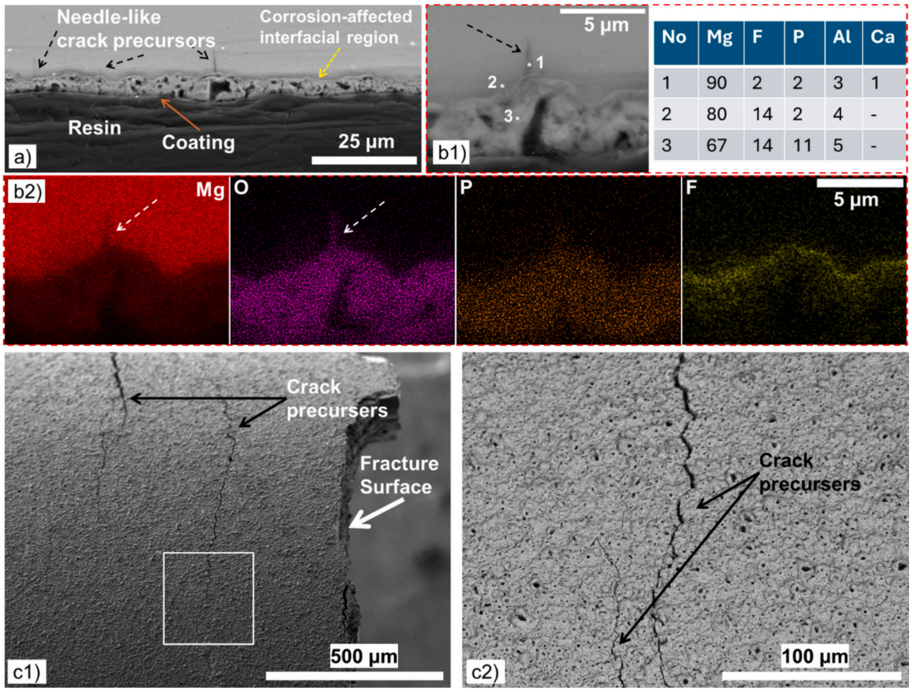

No	Mg	F	P	Al	Ca
1	90	2	2	3	1
2	80	14	2	4	-
3	67	14	11	5	-

Fig. 9. Needle-like crack precursors revealed by cross-sectional SEM/EDS and tensile-surface imaging. (a) Cross-section from a 5 µm ECO-coated, non-corroded AZ31 rod interrupted at 25,000 cycles (tensile side near the loading pin). (b1) High-magnification view of one precursor and representative EDS point analyses (wt%) at locations 1–3. (b2) Elemental maps (Mg, O, P, F) across the precursor. (c1) Tensile surface of a 15 µm-coated specimen that fractured at 59,000 cycles; the boxed area is enlarged in (c2).

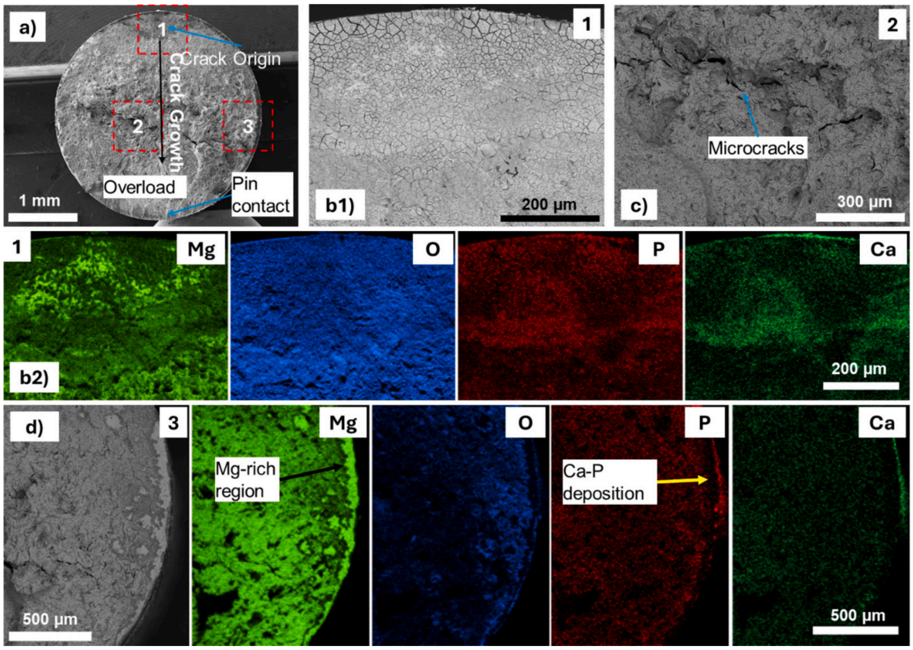

Fig. 10. Fracture surface and chemistry of uncoated X0 after 1 week of pre-corrosion and subsequent 3 PB fatigue failure. (a) Whole fracture section showing the crack origin, crack-growth direction, final-overload region, and pin-contact zone; red dashed boxes indicate Areas 1–3. (b1) Higher-magnification view of Area 1. (b2) Corresponding EDS maps (Mg, O, P, and Ca). (c) Area 2 near the neutral axis. (d) Area 3 near the edge close to the neutral axis, with corresponding EDS maps.

surface, numerous needle-like crack precursors were present (Fig. 11b1). EDS maps showed the precursors and the main crack to be oxygen-rich with a corresponding decrease in Mg signal along the same paths (Fig. 11b2–b3).

To document fatigue damage, three tensile-side cross-sections were prepared and polished nearly to mid-thickness (~1.5 mm removal) from: (a) an uncoated X0 specimen examined after failure, (b) a 5 µm ECO-coated specimen interrupted before fracture, and (c) a 15 µm ECO-coated specimen interrupted before fracture (Fig. 12). In the uncoated sample (Fig. 12a), two secondary cracks are visible adjacent to the main fracture surface; both initiate from the tensile surface and extend toward the neutral axis. The accompanying EDS maps and spectrum analysis show a strong O signal along the crack walls and near the free surface, while the Mg signal is depleted only within the crack paths (Table 3-

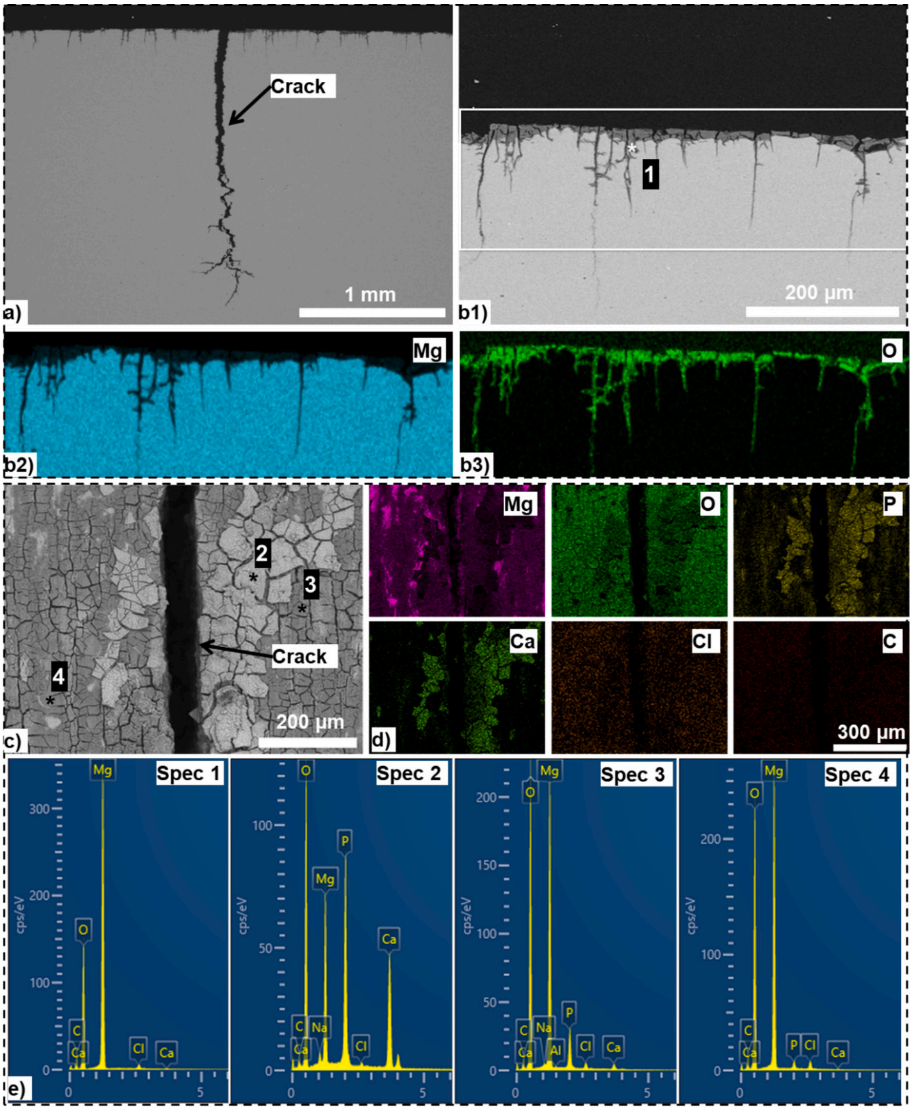

Fig. 11. Cross-sectional SEM/EDS analysis of uncoated, non-pre-corroded X0 after three-point bending fatigue. (a) Low-magnification cross-section. (b1) Higher-magnification view of the tensile-side region. (b2–b3) Corresponding EDS maps. (c) BSE image of the surface showing the main crack and adjacent deposits; numbered spectrums (specs1–4) indicate the locations of point analyses. (d) Elemental maps (Mg, O, P, Ca, Cl, and C). (e) Representative EDS spectra acquired from the marked locations.

Point 1). In the 5 μm-coated sample (Fig. 12b), multiple needle-like crack precursors emerge from the tensile surface. A corrosion-affected zone is present immediately beneath the coating and at the coating/substrate interface with O enrichment associated with the intrusions and the interfacial band (Table 3-Point 2 and 3). Point 2, acquired from the corrosion-affected alloy region, exhibits elevated Mg and O contents, whereas Point 3 was acquired on the ECO coating and shows the presence of P, F, and Ca together with lower Mg and O. In the 15 μm-coated sample (Fig. 12c), local delamination is observed within/along the coating near the tensile edge together with an O-rich product layer at the outer surface. The separation is localised and was recorded at a position away from the pin-contact region. Point 4 corresponds to the underlying alloy, whereas Point 5 corresponds to the coating region associated with the delamination feature.

3.6.3. Static test

Under static loading at 50 N (elastic region), the uncoated sample exhibited crack initiation from a single point, followed by propagation, indicating the presence of a deep crack origin. Within this region at the surface, oxidized areas as well as Ca—P enriched deposits were detected. These deposits were located inside cavities which were lined by an inner layer containing Mg—O rich oxide phases.

In contrast, in the 15 μm coated sample, crack initiation was less severe, appearing as a number of fine micro-cracks. On this side there was a uniform layer of Ca—P and less evidence of deep pitting that was seen on the uncoated sample. A reduction in coating thickness was also observed at the tensile side, suggesting localised degradation under loading. The compression side was not examined in detail, since pitting effects are likely to cause extensive corrosion and deformation in that region.

Under static loading in the plastic regime after 2 weeks, the uncoated AZ31 (N0) sample showed a major crack initiated at the tensile side that propagated toward the compression side. This was accompanied by localised material degradation and cavity formation. In the 15 μm coated AZ31 (N3) sample, only small cavities were observed at the tensile side, and no crack propagation across to the compression side was detected.

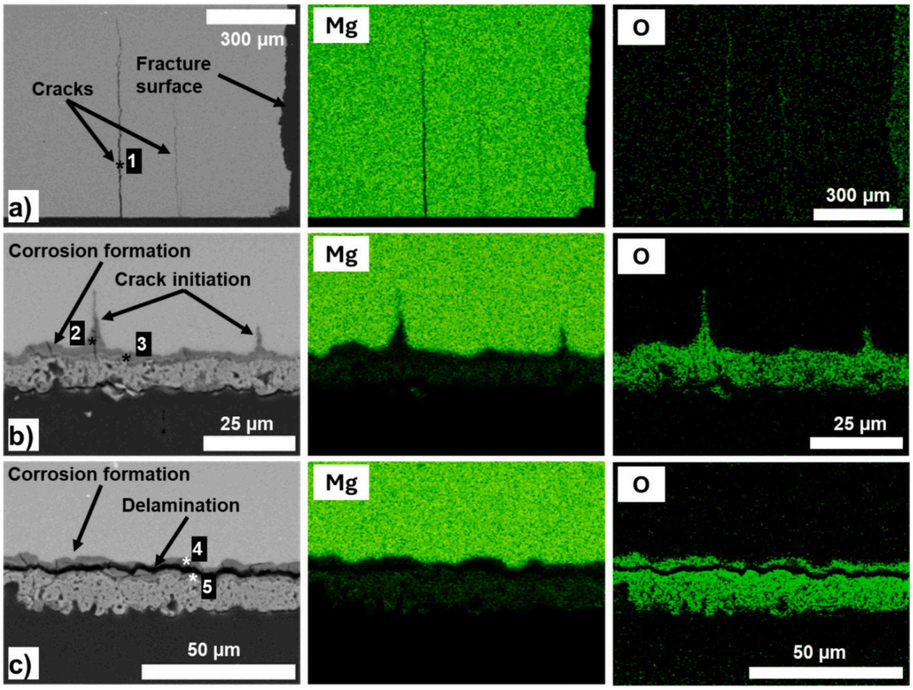

Fig. 12. Tensile-side cross-sections after three-point bending testing with corresponding EDS maps. Left column: BSE-SEM; middle column: Mg map; right column: O map. (a) Uncoated X0 examined after failure. (b) 5 μm ECO-coated specimen interrupted before fracture. (c) 15 μm ECO-coated specimen interrupted before fracture. Numbered points (1–5) indicate locations selected for EDS point analysis; quantitative results are given in Table 3. Scale bars: (a) 300 μm, (b) 25 μm, and (c) 50 μm.

Table 3
EDS point-analysis results (wt%) at the numbered locations (Points 1–5) indicated in Fig. 12. Values are reported for Mg, O, P, F, and Ca only and normalized to 100 wt% after excluding minor elements (e.g., Cl/Na) where present. *Trace* denotes signals below reliable quantification from the available spectral readout.

Point	Mg (wt%)	O (wt%)	P (wt%)	F (wt%)	Ca (wt%)
Point 1	83.1	16.9	Trace	Trace	Trace
Point 2	43.6	51.0	3.1	2.3	Trace
Point 3	34.2	43.4	9.7	10.5	2.2
Point 4	67.9	23.7	3.9	3.9	0.60
Point 5	36.7	38.4	7.7	15.3	1.9

4. Discussion

The advantage of using implants made from magnesium alloys is that they degrade, thereby avoiding the need for a second operation to remove them. The corrosion rate for resorbable magnesium alloys used for biomedical applications is important as timing of their resorption must be coupled to the healing process. Various coatings have been applied to these alloys to control their degradation and reduce corrosion rates, thereby preventing premature failure. In this study, ECO coatings were applied to two different magnesium alloys, AZ31 and X0, at thicknesses of 5 and 15 μm to evaluate their performance under conditions relevant to physiological environments. Consistent with the nature of the electrochemical oxidation process, the coatings exhibited a porous microstructure with intrinsic cracks that could potentially act as preferential sites for localised degradation. The present findings demonstrate how these microstructural features, in combination with coating thickness, govern the corrosion behaviour, fatigue life, and susceptibility to stress corrosion cracking of Mg alloys when subjected to mechanical loading in a corrosive medium.

4.1. Microstructure and coating defects

In line with other SEM observations, ECO coatings exhibited characteristic cracks and pores that inherently limit the continuity of the protective barrier [29–31]. Compared with other surface treatments such as plasma electrolytic oxidation (PEO) or anodizing, ECO coatings are generally reported to produce fewer surface-related defects and microstructural irregularities; however, thermally driven processes can still generate a degree of surface roughness [30]. These microstructural imperfections including micro-cracks that penetrate the coating can act as preferential sites for electrolyte ingress and localised corrosion of the magnesium alloys [23,33]. Although some cracks may remain relatively passive depending on deformation of the underlying substrate, others can behave as active defects under mechano-chemical loading, facilitating coating breakdown [31].

Due to the plasma-discharge nature of ECO processing, coatings are non-uniform in thickness [34]. In our previous study [30], cross-sectional BSE imaging of AZ31 with PF coatings, nominally labelled as 5 μm and 15 μm, revealed actual mean thicknesses of 4.3 μm and 11.4 μm, respectively. Porosity analysis further confirmed that the PF 5 μm and 15 μm coatings exhibited average porosity levels of ~9% and ~15%, respectively [33,35,36]. Nevertheless, for X0 alloys, local morphological variations were more pronounced, and coating homogeneity was not always uniform across the surface. The electrochemical process varies according to the morphology and substrate composition and fine tuning of this process is required to produce optimal coatings. Importantly, however, full surface coverage was consistently achieved, ensuring that no substrate exposure occurred despite local variations in thickness.

While thicker coatings are generally considered to enhance corrosion resistance, previous studies have shown that excessive thickness may instead promote crack initiation at the coating–substrate interface [37]. The results presented here demonstrate that 15 μm ECO coatings offer long-term corrosion resistance under both static and fatigue loading conditions compared to uncoated AZ31. However, local thinning and micro-cracking at the tensile side indicate that thickness alone is insufficient to fully suppress crack-driven damage. Similar to the dense barrier layers described in anodic and PEO coatings [33], the fluorine-rich interfacial layer observed in our ECO coatings likely contributed to delaying the penetration of HBSS despite the porous outer structure [29]. This dual structure; an outer porous layer and an inner dense fluorine-rich layer, appears to play a key role in balancing the competing effects of protection versus vulnerability under physiological conditions.

Mechanical loading further amplifies the effect of coating defects. Under bending and sustained static load, which induces strain, pores and microcracks can open or coalesce, accelerating electrolyte penetration into the substrate [38]. This mechano-chemical coupling explains why, in our static loading experiments, uncoated AZ31 rapidly developed deep cracks initiating on the tensile surface, while 15 μm coated specimens exhibited only localised thinning and much finer microcracks at the tensile edge (Fig. 13b). These observations highlight the importance of evaluating these alloys and their coatings under combined mechanical and corrosive environments representative of physiological loading as coating effectiveness cannot be assessed solely under immersion conditions.

4.2. *Corrosion behaviour*

Gravimetric methods for assessing magnesium degradation are limited by the formation of adherent corrosion products, which mask the true material loss and can even lead to apparent weight gain [39]. In contrast, XCT enables separation of corrosion products from the metallic substrate and provides a more accurate quantification of volume change [40,41]. The limitations of gravimetric methods have been reported: ECO-coated AZ31 rods exposed to 2 weeks of immersion at room temperature showed no measurable weight loss for either uncoated or coated specimens, resulting in a calculated low corrosion rate of 10^{-5} mm/year [31]. Geometry effects may contribute to this outcome, as rod dimensions and exposed surface area strongly affect diffusion pathways, local pH gradients, and corrosion progression [42,43]. The rise in pH during immersion can promote temporary passivation by $Mg(OH)_2$ deposition, but non-uniform pH distribution across the surface may also drive localised corrosion [42,44]. Similarly, studies with disc specimens found no significant changes in corrosion rate after 14 days in HBSS, PBS, 4 × PBS, and saline solutions [29], highlighting the insensitivity of weight-loss measurements for assessing the corrosion rate during short-term exposure.

In the present work, XCT quantification after three weeks of immersion in HBSS revealed a thickness-dependent reduction in the corrosion rate for AZ31 rods, with values of $\approx$0.005 mm/year for uncoated, $\approx$0.0015 mm/year for 5 μm coated, and $\approx$0.001 mm/year for 15 μm coated specimens (Fig. 3). One uncoated sample was completely degraded before the post-immersion scan, further emphasising the severity of corrosion in the absence of ECO protection. Despite the observed trend of reduced corrosion with increasing coating thickness, statistical analysis (Kruskal–Wallis test, $p = 0.119$) did not indicate significant differences between groups. This outcome is most likely attributable to the small sample size, variability in localised attack, and the relatively short test duration. It should also be noted that once corrosion proceeds to the point where specimen dimensions are drastically reduced or the metal is perforated, as in the case of the fully degraded uncoated rod, the accuracy of corrosion rate calculations becomes uncertain, since the exposed area during testing no longer corresponds to the initial geometry [45].

These results confirm that ECO coatings reduce corrosion in AZ31 under physiological conditions, with the 15 μm coating providing the greatest benefit. However, the modest improvement between 5 μm and 15 μm coatings within the 3-week exposure period suggests that

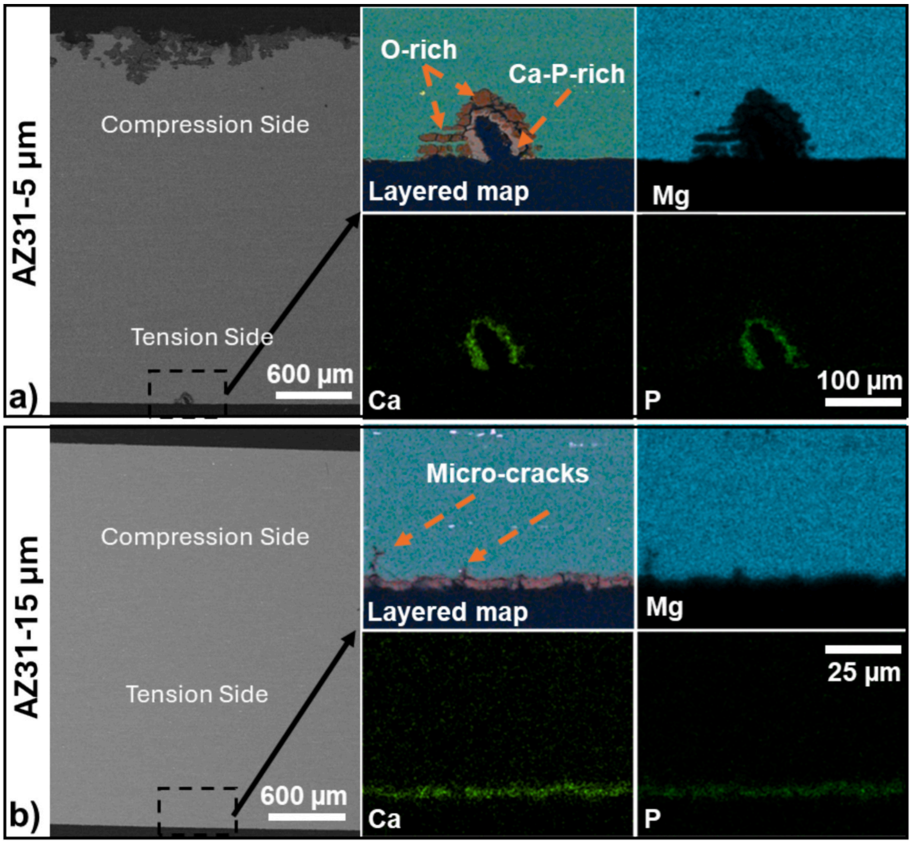

Fig. 13. Cross-sectional SEM images and corresponding EDS elemental maps of the tensile and compression sides of AZ31 specimens under static loading in the elastic regime. (a) Uncoated specimen. (b) 15 μm ECO-coated specimen. The maps show the elemental distributions in the regions of interest on the tensile and compression sides.

thickness alone is insufficient. Previous studies have shown that coating morphology and porosity can limit the additional benefits of thicker coatings [46–48]. This is consistent with the morphology of the coatings that we investigated, where local thinning and microcracks were seen in both thick and thin coatings that could lead to corrosion and this may have contributed to the only small difference seen between corrosion rates. Factors other than thickness which include porosity, coating uniformity, and defect morphology, are therefore key determinants of long-term corrosion resistance of ECO coated alloys in chloride-containing environments.

In a previous study by Yavuzyegit et al. [29], 15 μm ECO-coated AZ31 Mg alloys were exposed to 5 M NaCl solution at 37 °C for 2 weeks, and corrosion-related deposits were observed not only on the coating surface but also within coating pores and defects, with Mg- and O-rich regions indicating the accumulation of corrosion products within these local features. In a subsequent study by Yavuzyegit et al. [31], in situ three-point bending combined with high resolution digital image correlation and electron microscopy under plastic loading demonstrated that cracks within the coating could open, propagate through the full coating thickness, and reach the substrate under load. Taken together, these findings help explain the protective mechanism proposed in the present study. Specifically, the corrosion resistance of the 15 μm ECO coating appears to arise from a dual and condition-dependent mechanism. On the one hand, the coating acts as a barrier to fluid ingress; on the other hand, corrosion products may partially fill pores and microdefects within the coating and thereby act as a secondary barrier to fluid ingress. Mechanical loading can drive crack opening and through-thickness crack propagation, which locally compromises this protection by creating direct pathways to the underlying alloy. Therefore, the apparent long-term benefit of the thicker coating should not be interpreted as the effect of an entirely intact static barrier, but rather as the result of a dynamic balance between corrosion-product-assisted partial defect filling and mechanically induced crack evolution.

4.3. Mechanical properties and fatigue life

Fatigue behaviour of AZ31 alloys revealed clear dependencies on coating condition, corrosion history, and microstructural characteristics. In all AZ31 specimens, cracks consistently initiated at the tensile region and propagated toward the compressive (loading pin) side (Fig. 7a1-b1-c1, Fig. 10a), in line with the typical stress distribution in three-point bending. The initiation region was smooth, followed by a transition to dimpled morphology indicative of final overload. Uncoated AZ31 specimens displayed shallow pits at the crack origin, confirming that surface imperfections acted as preferential initiation sites. This aligns with the general understanding that fatigue fracture originates from local stress concentrations at defect sites [49,50] and that materials are weaker in tension than in compression. In conventional fatigue, such defects may arise internally, whereas in corrosion fatigue, they predominantly form on the surface from pits or cracks induced by corrosion [51]. As surface degradation progresses with immersion time, the associated stress concentrations increase and eventually trigger crack initiation, eliminating the possibility of an infinite fatigue life under corrosive conditions [52]. As this is a time-driven process, an endurance limit cannot be assigned under corrosive conditions.

Notably, no classical concentric fatigue striations were resolved on the fracture surfaces. This is expected under corrosion–fatigue conditions, because corrosion products and repeated film rupture/repassivation promote surface roughening and local dissolution, which can mask, degrade, or completely remove fine striation markings that would otherwise be observed in conventional fatigue fractography. Instead, the fracture appearance was dominated by pit/defect-controlled crack initiation and a rapid transition to dimpled overload features.

Fatigue-life comparisons indicate that, for AZ31, ECO coating did not provide a clear benefit at short exposure times. Under non-corroded conditions and after 1-week immersion in HBSS, the mean cycles to failure of coated rods were comparable to, or marginally lower than, those of uncoated AZ31, and differences were within scatter (Fig. 5; $p > 0.05$). This trend appears inconsistent with the lower corrosion rates measured for coated specimens by XCT at later time points [53], suggesting that in the early stage the fatigue response is governed less by bulk corrosion rate and more by near-surface mechanical factors introduced by the coating.

A plausible explanation is that the ECO process generates a mechanically less favourable surface condition than the machined surface of the uncoated alloy. The porous and locally brittle oxide layer, together with local thickness non-uniformity and an undulating coating–substrate interface, can act as a micro-notch under tensile loading in three-point bending. These discontinuities may elevate local stress concentrations and promote early crack nucleation within the coating, followed by rapid transmission into the AZ31 substrate, thereby offsetting any corrosion-mitigation benefit after 1 week of pre-exposure.

At first sight, the combination of a reduced corrosion rate and no corresponding improvement in fatigue life under non-corroded or short-term corrosive conditions appears contradictory; however, these responses are governed by different controlling mechanisms. The XCT data quantify global volumetric material loss of non-loaded specimens and show that ECO coatings, including the 5 μm condition, reduce the overall corrosion severity after immersion. By contrast, the early fatigue response is controlled primarily by local crack-initiation conditions at or near the tensile surface rather than by the average corrosion rate alone. In the present system, local coating defects, crack connectivity, and interfacial irregularities can dominate the fatigue response during the early stage of exposure, such that a reduction in bulk corrosion does not necessarily translate into improved fatigue resistance. This finding suggests that, for short-term implants or early-stage service conditions, optimising the microstructural integrity of the coating may be at least as important as reducing the average corrosion rate, because early failure is governed by defect-assisted crack initiation rather than by global material loss.

Importantly, the 15 μm coated AZ31 specimens immersed for 1 week exhibited abundant microvoids on fracture surfaces (Fig. 7-c2), whereas this feature was not prominent in the uncoated condition. These microvoids are consistent with hydrogen-assisted microvoid nucleation and coalescence under corrosion–fatigue [54]. In chloride-containing media, Mg corrosion generates hydrogen [55]; critically, hydrogen evolution is not necessarily confined to the external rod surface. In coated specimens, electrolyte ingress through open pores and coating cracks can drive localised corrosion reactions at, or near, the coating/substrate interface and deep within crack networks. Hydrogen generated in these occluded regions can become trapped within the porous coating, corrosion films, or interfacial zones, increasing local hydrogen activity and facilitating void nucleation during cyclic loading. This interpretation is also compatible with the broader literature; although Merson et al. [56] questioned whether diffusible hydrogen is the dominant driver of long-term pre-exposure embrittlement, they acknowledged that hydrogen retained within corrosion films or interfacial regions may still promote brittle cracking—consistent with the present observations.

In our ECO-coated AZ31 specimens, needle-like crack precursors enriched in oxygen and occasionally calcium were observed within and just beneath the porous ECO layer (Fig. 9a–c). These features likely reflect a synergy between local electrochemical activity and hydrogen-assisted decohesion. Although minor delamination was occasionally observed near the pin-contact region, widespread interfacial decohesion was absent, suggesting that failure was driven primarily by crack initiation within the coating and its subsequent transmission into the substrate rather than by loss of adhesion.

Notably, the 15 μm coated AZ31 specimens tested after 3 weeks of immersion exhibited markedly higher corrosion–fatigue resistance compared to their non-corroded and 1-week immersed counterparts. This counterintuitive trend may be attributed to the progressive formation of a relatively stable surface film during prolonged immersion. In particular, the growth of a $Mg(OH)_2$-rich layer within the porous ECO coating could act as a secondary barrier, filling surface defects. Similar self-sealing effects of corrosion products have been reported in PEO-coated Mg alloys, where the accumulation of hydroxide and phosphate phases blocked pores and cracks and temporarily enhances corrosion resistance [24,57,58]. Such in-situ sealing may therefore reduce electrolyte ingress and delay crack initiation under cyclic loading, thereby explaining the apparently improved fatigue resistance observed after extended immersion.

Although the improved performance of the 15 μm coating after prolonged immersion may be partially associated with corrosion-product-assisted sealing of pores or microcracks, this effect should not be interpreted as permanently stable or universally reliable. Any such self-sealing layer is likely to be condition-dependent and potentially temporary, because under continued chloride exposure or higher mechanical loading the deposited products may crack, dissolve, detach, or lose their barrier continuity. This interpretation is consistent with the present findings: while prolonged immersion may promote formation of a secondary surface barrier that delays electrolyte ingress, the coating still remains susceptible to localised degradation and does not fully prevent crack initiation under sustained loading. Therefore, the apparent self-sealing effect is more appropriately viewed as a mechanism that may delay, rather than permanently eliminate, corrosion-assisted damage, and its long-term reliability will depend on the balance between corrosion-product deposition, coating defect morphology, and the applied mechanical–environmental conditions. Biomedical applications of magnesium rely on the alloys degrading and the use of a coating that delays corrosion may prevent uncontrolled and premature degradation.

4.4. Static sustained loading and stress corrosion cracking (SCC)

Static loading experiments highlighted the dual role of ECO coatings in mediating SCC behaviour. In the elastic regime (50 N), uncoated AZ31 specimens exhibited distinct crack initiation at the tensile side, accompanied by oxidation and Ca—P deposition within surface cavities (Fig. 13a). These features indicate that local electrochemical activity promoted early-stage SCC under relatively low mechanical stress. By contrast, the 15 μm coated specimens developed only needle-like micro-cracks, where cross sections through the coating and elemental mapping confirmed partial thinning of the coating at the tensile side (Fig. 13b). This suggests that while ECO coatings reduce the severity of crack initiation, they remain vulnerable to localised degradation when subjected to sustained stress. The results are consistent with the role of the fluorine-rich interfacial barrier layer identified in Section 4.1, which delays electrolyte penetration but cannot fully prevent crack initiation under tensile load.

In the plastic regime (150 N) after two weeks in HBSS, a clear divergence emerged between coated and uncoated specimens. The uncoated AZ31 rods displayed major crack propagation from the tensile to the compressive side, with stepwise load drops (~70–80% reduction) reflecting catastrophic SCC growth across the section (Fig. 14a). In contrast, the 15 μm coated specimens retained a higher residual load (~25% reduction over 14 days) and showed only small cavities confined to the tensile edge, without through-thickness propagation (Fig. 14b). These observations emphasise that the coating, despite its inherent porosity and micro-cracks, was able to delay or suppress catastrophic SCC propagation.

Because the static 3 PB tests were performed under constant displacement, the observed decrease in load should be interpreted primarily as a progressive increase in specimen–system compliance rather than as a direct measure of corrosion-induced section loss alone (Fig. 6). At 50 N, the similar load reduction in coated and uncoated specimens suggests that different local damage mechanisms may produce a comparable overall decrease in stiffness under sustained displacement (Fig. 13). In the uncoated specimen, one plausible contributor was local material loss associated with the combined mechanical and corrosive effects, particularly in the region adjacent to the compression-side, which would reduce the effective support reaction under fixed displacement conditions (Fig. 13a). By contrast, this effect was not clearly evident in the coated specimen, where the tensile side instead showed multiple fine micro-cracks, consistent with distributed local damage and a modest time-dependent reduction in resistance (Fig. 13b). Under the 150 N condition, the mechanisms diverged more clearly: the uncoated specimens exhibited a major crack extending from the tensile side toward the compression side, together with local degradation and cavity formation, indicating catastrophic corrosion-assisted failure and a strong reduction in effective load-bearing capacity (Fig. 14a). In contrast, the 15 μm coated specimens showed only limited local cavities at the tensile side, while compression-side damage remained much more restricted and no crack propagated across the section (Fig. 14b). This suggests that the remaining load reduction in the coated group arose from increased compliance associated with local substrate plastic deformation and/or limited localised corrosion beneath damaged coating regions, rather than catastrophic section-spanning failure.

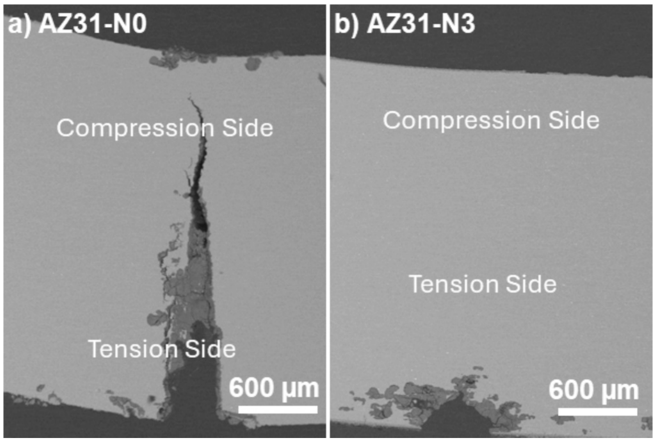

Fig. 14. Cross-sectional SEM images of AZ31 specimens after 2 weeks of exposure under plastic loading: (a) AZ31-N0 and (b) AZ31-N3.

Taken together, the results suggest that ECO coatings act primarily by limiting crack growth rather than completely preventing crack initiation. This behaviour is consistent with reports on other ceramic-like coatings such as PEO or anodic films, where brittle surface defects often trigger cracks but dense interfacial layers provide resistance to propagation [59]. The fluorine-rich inner barrier observed in ECO coatings likely contributes to this effect by restricting electrolyte ingress into the substrate. From an application perspective, these findings imply that while ECO coatings cannot fully eliminate SCC under static loading, they may extend implant longevity by slowing crack penetration across the section, particularly under plastic stresses representative of load-bearing conditions.

5. Conclusion

This study evaluated the role of ECO coatings on AZ31 and X0 magnesium alloys under physiologically relevant mechanical and corrosive environments. ECO coatings successfully reduced the corrosion rate of AZ31, with the 15 μm layer providing the greatest benefit. However, the protective effect was modest and strongly influenced by coating microstructural defects, thickness uniformity, and localised degradation.

Fatigue experiments revealed that cracks consistently initiated at the tensile edge, with initiation sites linked to pits and cracks in the coating. While coatings did not enhance fatigue life in non-corroded or short-term pre-corroded AZ31, the 15 μm ECO layer improved corrosion–fatigue resistance through in-situ defect sealing by $Mg(OH)_2$ deposition.

Sustained static loading highlighted the dual role of ECO coatings in stress corrosion cracking (SCC): although coatings reduced early crack initiation under elastic stress, only 15 μm thick coatings delayed catastrophic crack propagation under plastic loading. Fractography further indicated that hydrogen-assisted damage mechanisms, combined with surface defects, contributed to microvoid formation and accelerated crack initiation.

Overall, ECO coatings mitigate but do not eliminate the degradation of Mg alloys. Their long-term effectiveness in a corrosive environment is governed by the interplay between coating thickness, microstructural integrity, corrosion product sealing, hydrogen embrittlement, and loading. These insights underline the necessity of optimising ECO processing parameters and integrating mechanical–corrosive testing protocols to advance the safe clinical translation of Mg-based biomedical implants.

CRediT authorship contribution statement

Berzah Yavuzyegit: Writing – original draft, Visualization, Methodology, Investigation, Formal analysis, Conceptualization. **Katerina Karali:** Supervision, Funding acquisition, Formal analysis, Conceptualization. **Sarah Davis:** Writing – review & editing, Methodology, Investigation. **Kemal Balandiz:** Writing – review & editing, Methodology. **Lauren Jones:** Methodology. **Nigel Smith:** Writing – review & editing, Funding acquisition, Conceptualization. **Sergey Usov:** Methodology, Funding acquisition, Conceptualization. **Pavel Shashkov:** Methodology, Funding acquisition, Conceptualization. **Roxane Bonithon:** Writing – review & editing, Supervision, Methodology, Conceptualization. **Gordon Blunn:** Writing – review & editing, Supervision, Methodology, Investigation, Funding acquisition, Formal analysis, Conceptualization.

Ethical approval

Not applicable.

Declaration of competing interest

The authors declare the following financial interests/personal relationships which may be considered as potential competing interests:

Pavel Shashkov, Gennady Khomutov, Aleksey Yerokhin, Sergey Usov has patent #PCT Patent WO2012107754 licensed to BioCera Medical Limited. If there are other authors, they declare that they have no known competing financial interests or personal relationships that could have appeared to influence the work reported in this paper.

Acknowledgements

This work was supported by Innovate UK [10025764]. We gratefully acknowledge Geoff Britton, Colin Lupton, and Joseph Dunlop for technical assistance from the University of Portsmouth.

Appendix A. Supplementary data

Supplementary data to this article can be found online at https://doi.org/10.1016/j.surfcoat.2026.133511.

Data availability

Data will be made available on request.

References

[1] K. Takata, M. Yugami, S. Karata, T. Karasugi, Y. Uehara, T. Masuda, T. Nakamura, T. Tokunaga, S. Hisanaga, K. Sugimoto, Plates made from magnesium alloy with a long period stacking ordered structure promote bone formation in a rabbit fracture model, Sci. Rep. 15 (2025) 12210.
[2] Z. Shan, X. Xie, X. Wu, S. Zhuang, C. Zhang, Development of degradable magnesium-based metal implants and their function in promoting bone metabolism (a review), J. Orthop. Transl. 36 (2022) 184–193.
[3] A. Rezaei-Baravati, M. Kasiri-Asgarani, H.R. Bakhsheshi-Rad, M. Omidi, E. Karamian, S. Abazari, S. Sharif, A.F. Ismail, J.W. Drelich, Mechanical properties, biodegradation, and biocompatibility of porous Mg alloy scaffolds for load bearing bone applications, J. Mater. Eng. Perform. 34 (2025) 16348–16360.
[4] J.W. Drelich, J. Goldman, Bioresorbable vascular metallic scaffolds: current status and research trends, Curr. Opin. Biomed. Eng. 24 (2022) 100411.
[5] M. Ramya, Advances in biodegradable orthopaedic implants: optimizing magnesium alloy corrosion resistance for enhanced bone repair, Biomed. Mater. Devices 3 (2025) 396–414.
[6] J.S. Suh, B.-C. Suh, J.H. Bae, Y.M. Kim, Machine learning-based design of biodegradable Mg alloys for load-bearing implants, Mater. Des. 225 (2023) 111442.
[7] J.S. Suh, J.H. Jang, B.-C. Suh, J.-Y. Kim, Reverse design of Mg-Zn-Mn-Sr-Ca alloys for biodegradable implants by interpretable machine learning and genetic algorithm, Mater. Des. 114494 (2025).
[8] L. Choudhary, R.K.S. Raman, Magnesium alloys as body implants: fracture mechanism under dynamic and static loadings in a physiological environment, Acta Biomater. 8 (2012) 916–923.
[9] R.K. Singh Raman, L. Choudhary, Cracking of magnesium-based biodegradable implant alloys under the combined action of stress and corrosive body fluid: a review, Emerging Mater. Res. 2 (2013) 219–228.
[10] S. Kamrani, C. Fleck, Biodegradable magnesium alloys as temporary orthopaedic implants: a review, Biometals 32 (2019) 185–193.
[11] P. Das, T.S.S. Kumar, K.K. Sahu, S. Gollapudi, Corrosion, stress corrosion cracking and corrosion fatigue behavior of magnesium alloy bioimplants, Corros. Rev. 40 (2022) 289–333.
[12] S. Jafari, S.E. Harandi, R.K. Singh Raman, A review of stress-corrosion cracking and corrosion fatigue of magnesium alloys for biodegradable implant applications, Jom 67 (2015) 1143–1153.
[13] M. Sabbaghian, S. Arbabi, R. Mahmudi, Stress corrosion cracking and bio-corrosion behavior of Mg–TiO2 composites, Mater. Today Commun. 49 (2025) 113922.
[14] Y. Luo, F. Liu, Z. Chen, Y. Luo, W. Li, J. Wang, A magnesium screw with optimized geometry exhibits improved corrosion resistance and favors bone fracture healing, Acta Biomater. 178 (2024) 320–329.
[15] H. Ibrahim, C. Billings, M. Abdalla, A. Korra, D.E. Anderson, In vivo assessment of high-strength and corrosion-controlled magnesium-based bone implants, Bioengineering 10 (2023) 877.
[16] I. Antoniac, V. Manescu, A. Antoniac, G. Paltanea, Magnesium-based alloys with adapted interfaces for bone implants and tissue engineering, Regen. Biomater 10 (2023) rbad095.
[17] S. Zhao, M. Tayyebi, M. Yarigarravesh, G. Hu, A review of magnesium corrosion in bio-applications: mechanism, classification, modeling, in-vitro, and in-vivo experimental testing, and tailoring Mg corrosion rate, J. Mater. Sci. 58 (2023) 12158–12181.
[18] L. Chen, Y. Sheng, H. Zhou, Z. Li, X. Wang, W. Li, Influence of a MAO+ PLGA coating on biocorrosion and stress corrosion cracking behavior of a magnesium alloy in a physiological environment, Corros. Sci. 148 (2019) 134–143.
[19] M. Abdalla, A. Joplin, M. Elahinia, H. Ibrahim, Corrosion modeling of magnesium and its alloys for biomedical applications, Corros. Mater. Degrad. 1 (2020) 11.
[20] L. Wei, Z. Gao, Recent research advances on corrosion mechanism and protection, and novel coating materials of magnesium alloys: a review, RSC Adv. 13 (2023) 8427–8463.
[21] X. Qi, Z. Zhuo, Y. He, X. Su, C. Yang, B. Jiang, R. Song, Effect of an MAO/PMTMS composite coating on the electrochemical corrosion and stress corrosion cracking behavior of an AZ80 magnesium alloy, Corros. Sci. 257 (2025) 1–15, 113308.
[22] X. Guo, Y. Hu, K. Yuan, Y. Qiao, Review of the effect of surface coating modification on magnesium alloy biocompatibility, Materials (Basel). 15 (2022) 3291.
[23] J. Nachtsheim, S. Ma, J. Burja, B. Markert, In vitro evaluation of stress corrosion cracking susceptibility of PEO-coated rare-earth magnesium alloy WE43, Surf. Coat. Technol. 477 (2024) 130391.
[24] A. Ghanbari, A. Bordbar-Khiabani, F. Warchomicka, C. Sommitsch, B. Yarmand, A. Zamanian, PEO/polymer hybrid coatings on magnesium alloy to improve biodegradation and biocompatibility properties, Surf. Interfaces 36 (2023) 102495.
[25] N. Li, N. Ling, H. Fan, K. Liang, J. Zhang, L. Wang, Smart functionalization of PEO coating on AZ31B magnesium alloy by a novel facile one-step sealing method, Surf. Coat. Technol. 467 (2023) 129674.
[26] C. Yang, P. Chen, W. Wu, L. Sheng, Y. Zheng, P.K. Chu, A review of corrosion-resistant PEO coating on Mg alloy, Coatings 14 (2024) 451.
[27] Y.Q. Almajidi, E. Ali, M.F. Jameel, L.H. Saleh, S. Aggarwal, S.A. Zearah, A. F. Alamula, A. Alsaalamy, F. Sharifianjazi, Unveiling the Effect of Particle Incorporation in PEO Coatings on the Corrosion and Wear Performance of Magnesium Implants, 2023, pp. 1–35.
[28] Y.C. Ma, H.Y. Tang, Y. Zhang, S. Zhang, Q. Wang, T. Zhang, J. Ma, Effect of high glucose environment on stress corrosion cracking behavior of plasma electrolytic oxidation coated Mg-0.45 Ca-0.45 Zn alloy, Surf. Coat. Technol. 512 (2025) 1–13, 132358.

[29] B. Yavuzyegit, A. Karali, A. De Mori, N. Smith, S. Usov, P. Shashkov, R. Bonithon, G. Blunn, Evaluation of corrosion performance of AZ31 Mg alloy in physiological and highly corrosive solutions, ACS Appl. Bio Mater. 7 (2024) 1735–1747, https://doi.org/10.1021/acsabm.3c01169.
[30] B. Yavuzyegit, K. Karali, E. Avcu, A. De Mori, D. Quizon, M. Hacıosmanoğlu, A. P. Hekimoğlu, N. Smith, S. Usov, P. Shashkov, R. Bonithon, G. Blunn, Corrosion and mechanical performance of novel electrochemical oxidation coatings on AZ31 magnesium alloys for biomedical applications, Surf. Coat. Technol. 507 (2025), https://doi.org/10.1016/j.surfcoat.2025.132151.
[31] B. Yavuzyegit, K. Karali, S. Davis, B. Morrison, S. Karabal, K. Balandiz, N. Smith, S. Usov, P. Shashkov, R. Bonithon, G. Blunn, High-resolution DIC analysis of in situ strain and crack propagation in coated AZ31 magnesium alloys under mechanical loading, J. Mater. Sci. 60 (2025) 14708–14730, https://doi.org/10.1007/s10853-025-11243-4.
[33] Y. Xiong, Y. Shen, L. He, Z. Yang, R. Song, Stress corrosion cracking behavior of LSP/MAO treated magnesium alloy during SSRT in a simulated body fluid, J. Alloys Compd. 822 (2020) 153707.
[34] C.-C. Huang, H.-M. Li, Effect of graphene addition during micro-arc oxidation process on wear and corrosion properties of composite oxide layers, Prot. Met. Phys. Chem. Surfaces 59 (2023) 179–190.
[35] H. Tian, Y. Zhang, X. Hao, H. Zhang, W. Wu, G. Han, Z. Dou, Y. Wei, Y. Zhang, F. Chen, Preparation and characterization of the low-energy plasma electrolysis oxide coatings on MgLi alloy, Surf. Coat. Technol. 440 (2022) 128445.
[36] A. Rajabi, S.M. Mousavi Khoei, R. Riahifar, T. Shahalizade, In-Situ Mos2-Modified Peo-derived Tio2 as a Carbon and Binder-free Anode for Li-Ion Batteries, Available SSRN 5256449 (n.d.).
[37] Y. Zou, Y. Wang, D. Wei, Q. Du, J. Ouyang, D. Jia, Y. Zhou, In-situ SEM analysis of brittle plasma electrolytic oxidation coating bonded to plastic aluminum substrate: microstructure and fracture behaviors, Mater. Charact. 156 (2019) 109851.
[38] P.B. Srinivasan, C. Blawert, W. Dietzel, Effect of plasma electrolytic oxidation treatment on the corrosion and stress corrosion cracking behaviour of AM50 magnesium alloy, Mater. Sci. Eng. A 494 (2008) 401–406.
[39] K.X. Kuah, D.J. Blackwood, W.K. Ong, M. Salehi, H.L. Seet, M.L.S. Nai, S. Wijesinghe, Analysis of the corrosion performance of binder jet additive manufactured magnesium alloys for biomedical applications, J. Magnesium Alloys 10 (2022) 1296–1310.
[40] M. Bandiera, A. Bonfanti, F. Bertasi, A. Mancini, High-resolution CT Scan as Tool for Precise Quantification of Material Loss due to Localized Corrosion in Brake Calipers, NACE Corros., NACE, 2021 p. D091S035R001.
[41] A. Ganesan, R. Springer, A. Howell, B. Burns, D.M. Hall, High-resolution X-ray computerized tomography to characterize localized corrosion rates of carbon steel in contaminated steam cycles, Npj Mater. Degrad. 9 (2025) 8.
[42] M.R. Sahu, A. Yamamoto, Investigating the effect of thickener concentrations on the corrosion behavior of pure Mg, J. Biomed. Mater. Res. Part A 113 (2025) e37878.
[43] L. Prince, X. Noirfalise, Y. Paint, M. Olivier, Corrosion mechanisms of AZ31 magnesium alloy: importance of starting pH and its evolution, Mater. Corros. 73 (2022) 1615–1630.
[44] H. Hornberger, H. Kissel, B. Striegl, M. Kronseder, F. Vollnhals, S. Christiansen, Bioactivity and corrosion behavior of magnesium barrier membranes, Mater. Corros. 73 (2022) 8–19.
[45] F. Malaret, X.-S. Yang, Exact calculation of corrosion rates by the weight-loss method, Exp. Results 3 (2022) e13.
[46] D. Zhang, F. Peng, J. Qiu, J. Tan, X. Zhang, S. Chen, S. Qian, X. Liu, Regulating corrosion reactions to enhance the anti-corrosion and self-healing abilities of PEO coating on magnesium, Corros. Sci. 192 (2021) 109840.
[47] R. Del Olmo, E. López, E. Matykina, U. Tiringer, J.M.C. Mol, M. Mohedano, R. Arrabal, Hybrid PEO/sol-gel coatings loaded with Ce for corrosion protection of AA2024-T3, Prog. Org. Coat. 182 (2023) 107667.
[48] A. Fattah-Alhosseini, R. Chaharmahali, M. Kaseem, Corrosion behavior amelioration of Ti-based alloys by the hybrid plasma electrolytic oxidation (PEO)/polymer coatings: a review, Hybrid Adv. 5 (2024) 100151.
[49] S.E. Harandi, R.K.S. Raman, Corrosion fatigue of a magnesium alloy under appropriate human physiological conditions for bio-implant applications, Eng. Fract. Mech. 186 (2017) 134–142.
[50] Z. Li, A.A. Luo, Q. Wang, H. Zou, J. Dai, L. Peng, Fatigue characteristics of sand-cast AZ91D magnesium alloy, J. Magnesium Alloys 5 (2017) 1–12.
[51] M. Liu, J. Wang, S. Zhu, Y. Zhang, Y. Sun, L. Wang, S. Guan, Corrosion fatigue of the extruded Mg–Zn–Y–Nd alloy in simulated body fluid, J. Magnesium Alloys 8 (2020) 231–240.
[52] Z.Y. Nan, S. Ishihara, T. Goshima, Corrosion fatigue behavior of extruded magnesium alloy AZ31 in sodium chloride solution, Int. J. Fatigue 30 (2008) 1181–1188.
[53] Y. Gao, A. Yerokhin, A. Matthews, Mechanical behaviour of cp-magnesium with duplex hydroxyapatite and PEO coatings, Mater. Sci. Eng. C 49 (2015) 190–200.
[54] S.-J. Huang, V. Rajagopal, V. Skripnyuk, E. Rabkin, C. Fang, A comparative study of hydrogen storage properties of AZ31 and AZ91 magnesium alloys processed by different methods, J. Alloys Compd. 935 (2023) 167854.
[55] P.S. Rodrigues, I.R. Zenóbio, T.I. da Silva, C.Q.C. Fernandes, T.G. de Sousa, J.A. de Castro, G.S. da Fonseca, J.A.O. Huguenin, E.A. Ferreira, Effect of aging on corrosion resistance of AZ31 magnesium alloy, J. Mater. Eng. Perform. 33 (2024) 3413–3425.
[56] E. Merson, V. Poluyanov, P. Myagkikh, D. Merson, A. Vinogradov, On the role of pre-exposure time and corrosion products in stress-corrosion cracking of ZK60 and AZ31 magnesium alloys, Mater. Sci. Eng. A 806 (2021) 140876.
[57] A. Alabbasi, A. Mehjabeen, M.B. Kannan, Q. Ye, C. Blawert, Biodegradable polymer for sealing porous PEO layer on pure magnesium: an in vitro degradation study, Appl. Surf. Sci. 301 (2014) 463–467.
[58] H. Sampatirao, S. Radhakrishnapillai, S. Dondapati, E. Parfenov, R. Nagumothu, Developments in plasma electrolytic oxidation (PEO) coatings for biodegradable magnesium alloys, Mater. Today Proc. 46 (2021) 1407–1415.
[59] S. Jafari, R.K.S. Raman, In-vitro biodegradation and corrosion-assisted cracking of a coated magnesium alloy in modified-simulated body fluid, Mater. Sci. Eng. C 78 (2017) 278–287.